S & M 4213

# Intelligent Optimal Scheduling of Wind-Photovoltaic-Storage Microgrid with Electric Vehicles

Zirui Zhang,<sup>1</sup> Keying Li,<sup>2</sup> Yuexi Ning,<sup>3</sup> Cheng-Jian Lin,<sup>4\*</sup> and Lingling Li<sup>5</sup>

<sup>1</sup>School of International Education, Hebei University of Technology, Tianjin 300401, China
 <sup>2</sup>School of Health Sciences & Biomedical Engineering, Hebei University of Technology, Tianjin 300401, China
 <sup>3</sup>School of Mathematical Science, University of Science and Technology of China, Hefei 230026, China
 <sup>4</sup>Department of Computer Science & Information Engineering, National Chin-Yi University of Technology, Taichung 411, Taiwan

<sup>5</sup>State Key Laboratory of Reliability and Intelligence of Electrical Equipment, Hebei University of Technology, Tianjin 300401, China

(Received July 23, 2025; accepted October 23, 2025)

*Keywords:* multi-source data fusion, LSTM-DLinear, Red-billed Blue Magpie Optimization (RBMO) Algorithm, microgrid scheduling, electric vehicles, price-responsive control

To address uncertainty challenges in highly renewable microgrids with large-scale electric vehicle (EV) integration, in this study, we developed a multi-source data-driven cooperative scheduling framework for wind-photovoltaic-storage-EV systems. The model integrates heterogeneous real-time monitoring data (grid status, renewable generation, and EV charging) through a Kalman-filter-based fusion architecture with dynamic anomaly detection. Renewable output and load uncertainties are predicted using a long short-term memory network (LSTM)-DLinear hybrid model combining DLinear's decomposition efficiency with LSTM's residual correction. The scheduling optimization employs the Red-billed Blue Magpie Optimization Algorithm to solve a four-dimensional economic objective ( $TEB = C_{procure} + RBE + B_{carbon} +$  $R_{lifecvcle}$ ) using gene-encoded 96-period decision variables. Key innovations include a priceresponsive EV charging mechanism with adjustable power boundaries  $(P_{ev}^{\min}(t) = \alpha(t))$  Prated and temporal energy constraints. Implemented through a closed-loop predict-then-optimize framework with day-ahead planning and real-time correction layers, the solution demonstrates an 18.9% reduction in renewable curtailment and a 42% economic benefit improvement in high-EV penetration scenarios. This research validates the critical role of multi-source sensor data fusion in enhancing grid flexibility and schedulability, providing an effective real-time optimization approach for highly renewable microgrids.

#### 1. Introduction

Driven by global carbon neutrality goals and the emission reduction constraints of the 2016 Paris Agreement, low-carbon energy transition has become a core strategic task for nations worldwide. Currently, more than 130 countries have pledged to achieve carbon neutrality before

<sup>\*</sup>Corresponding author: e-mail: <a href="mailto:cjlin@ncut.edu.tw">cjlin@ncut.edu.tw</a> <a href="mailto:https://doi.org/10.18494/SAM5858">https://doi.org/10.18494/SAM5858</a>

2050, with frameworks such as the EU's "Fit for 55" policy package and China's "dual-carbon" strategy driving profound transformations in energy systems. (1) International Energy Agency data indicate that global renewable energy investment surpassed \$1.8 trillion in 2023, yet the power sector still contributes 38% of global carbon emissions. As a critical enabler for UN Sustainable Development Goal 7 (SDG7), distributed energy systems, leveraging their proximity to load centers and high compatibility with renewable energy, have been incorporated into national energy transition roadmaps by major economies such as the US, Germany, and Japan. Global distributed photovoltaic (PV) installed capacity has maintained a compound annual growth rate of 21% over the past five years, historically exceeding 500 GW in 2023, signifying a leap in energy supply architecture from centralized to hybrid centralized-distributed models. (2)

The deep decarbonization and digitalization of global energy systems are reshaping power system operational paradigms through the large-scale integration of distributed renewable energy and electric vehicles (EVs). Clean energy sources such as wind and solar, benefiting from wide distribution characteristics and continuously declining costs, are rapidly proliferating in microgrid applications, but their inherent intermittency and uncertainty pose severe challenges to dispatching systems. Under high-penetration scenarios, renewable energy output fluctuations intensify pressure on energy storage systems, with frequent power imbalances threatening power quality. Concurrently, EVs, acting as novel loads and potential distributed energy storage resources, impose higher demands on microgrid flexibility and stability while advancing sensor improvement.<sup>(3)</sup>

Scholars worldwide have conducted extensive research on microgrid dispatching incorporating renewable energy. In addressing forecasting challenges, Zeng et al. questioned Transformers' efficacy in long-term time series forecasting (LTSF), proposing LTSF-Linear—a simple linear direct multi-step (DMS) baseline. (4) This study surpasses all Transformers across nine real datasets (20-50% average gain), exposing critical flaws. Transformers' permutation invariance causes sequential information loss, while existing studies rely on error-accumulating iterative prediction and unjustified complex architectures. (4) Abdelghany et al. proposed a model predictive control (MPC)-based hybrid storage system using simplified mixed logical dynamical (MLD) modeling, achieving 25% lower operating costs and 1500 fewer annual device switches. (5) However, it depends on commercial solvers and lacks uncertainty modeling or multi-objective validation. Hu et al. developed a two-stage prediction framework [RF/maximal information coefficient (MIC) feature reduction, gated recurrent units (GRU)/piecewise autoregressive with extra inputs (PWARX) models], identifying four critical turbines and achieving ≤3.76% normalized root mean square error (NRMSE) with > 95% interval coverage on North China wind farms.<sup>(6)</sup> Its computational intensity and terrain dependency limit broader applicability.<sup>(6)</sup> Li et al. introduced hybrid improved multi-verse optimizer support vector machine (HIMVO-SVM) (integrating chaotic mapping and differential evolution (DE) for SVM optimization), reducing MSE by 0.0026-0.0030 and MAPE by 1.98-3.68% versus benchmarks across weather conditions.<sup>(7)</sup> Accuracy declines during low-generation periods, and scalability is constrained by basic meteorological inputs. (7) Hochreiter and Schmidhuber proposed long short-term memory network (LSTM) with gating mechanisms to resolve recurrent neural network (RNN) vanishing gradients, enabling the robust learning of long-term dependencies. (8) Early scalability was constrained by computational inefficiency, parameter sensitivity, and limited empirical validation under noise. While Teixeira *et al.* successfully synthesized hybrid forecasting models that reduce errors, their work also revealed critical limitations. Specifically, their approach, which integrated decomposition with LSTM networks and was optimized by genetic algorithms, leveraged climatic data and preprocessing to lower the MAPE by 14.5%. Nevertheless, the study concluded that major challenges remain in addressing ultrashort-term intermittency, reducing computational demands for real-time operation, and enabling effective transfer learning to data-scarce regions. Scalability and practical validation remained insufficiently addressed.

On the other hand, regarding dispatching optimization methods, intelligent optimization algorithms are gradually replacing traditional tools owing to their strong search capabilities, with particle swarm optimization, (10) genetic algorithms, and grey wolf optimization (11) achieving favorable results in microgrid energy management. Particularly in complex scenarios involving multiple objectives, constraints, and dynamic environments, emerging algorithms such as whale optimization, firefly algorithm, and differential evolution exhibit promising performance. (12) Notably, in recent years, the nature-inspired Red-billed Blue Magpie Optimization (RBMO) Algorithm has attracted increasing attention in the dispatching optimization field owing to its ability to balance global exploration and local exploitation. (13)

Simultaneously, concerning EV integration scheduling, some research has modeled EVs as flexible loads. (14) Several studies focus on scheduling strategies for the vehicle-to-grid (V2G) mode, but are confronted with issues such as some EVs lacking discharge capability or limited user participation. (14) As for models considering only charging-side control, their integration within the multi-source coordination context of microgrids remains insufficient, particularly regarding synchronization with the volatility of renewable energy output. (14)

Against this backdrop, constructing an advanced energy dispatching system leveraging synergistic wind–solar–storage–EV multi-source data represents a critical breakthrough. Traditional dispatching methods exhibit significant limitations in addressing renewable energy output uncertainty and EV behavioral complexity, particularly lacking effective fusion capabilities for multi-timescale heterogeneous data (e.g., second-level charging data and minute-level renewable power data), thus struggling to meet the triple demands of modern microgrids for precision, adaptability, and real-time performance.

Consequently, developing a synergistic dispatching model that integrates multi-source monitoring sensors' data—including grid operational status, renewable energy output, and EV charging operations—and combines high-precision forecasting with intelligent decision-making, holds substantial theoretical value and practical significance.<sup>(3)</sup>

# 2. System Model

# 2.1 LSTM-DLinear hybrid forecasting model

Conventional prediction approaches exhibit significant limitations in time-series forecasting, as evidenced by the comparative analysis in Table 1. Traditional LSTM models suffer from

Table 1 Comparative analysis of prediction model limitations.

	*	
Model	Deficiencies	Fundamental Cause
LSTM	Degraded long-term accuracy	Vanishing historical context
DLinear	Limited nonlinear adaptation	Fixed linear decomposition
Statistical	Rigid pattern representation	Prescribed mathematical forms

degraded long-term accuracy due to vanishing historical context, while DLinear architectures demonstrate limited nonlinear adaptation stemming from fixed linear decomposition. Statistical methods further exhibit rigid pattern representation constrained by prescribed mathematical forms.

To overcome these limitations, the proposed LSTM-DLinear hybrid architecture integrates three core capabilities: DLinear's efficient trend-seasonal decomposition, LSTM's nonlinear residual learning, and attention-based temporal feature weighting. This synthesis enables robust pattern capture while maintaining sensitivity to complex temporal dependencies.

## 2.1.1 DLinear decomposition module

The decomposition module first extracts trend components through moving average filtering. (15)

$$\mathfrak{F}(t) = \frac{1}{k} \sum_{i=t-k/2}^{t+k/2} P(i) \tag{1}$$

Seasonal patterns are subsequently isolated using Seasonal-trend decomposition using Loess (STL) with diurnal periodicity:

$$\mathfrak{S}(t) = STL(P(t), period = T_{day}),$$
 (2)

where  $T_{day} = 24$  h for diurnal cycles.

Baseline prediction:

$$\hat{P}_{DLinear}(t+1) = \mathfrak{F}(t) + \mathfrak{S}(t). \tag{3}$$

## 2.1.2 LSTM-attention residual correction

The LSTM processes are as follows.

residuals 
$$r(t) = P(t) - \hat{P}_{DLinear}(t+1)$$
:  

$$i_t = \sigma(W_i[h_{t-1}, r_t] + b_i)$$

$$f_t = \sigma(W_f[h_{t-1}, r_t] + b_f)$$

$$o_t = \sigma(W_o[h_{t-1}, r_t] + b_o)$$

$$\tilde{C}_t = \tanh(W_C[h_{t-1}, r_t] + b_C)$$

$$C_t = f_t \odot C_{t-1} + i_t \odot \tilde{c}_t$$

$$h_t = o_t \odot \tanh(C_t)$$

$$(4)$$

An attention mechanism dynamically weights temporal features across hidden states.

$$\alpha_t = \operatorname{softmax} \left( u^{\mathsf{T}} \tanh \left( W_h h_t + b_h \right) \right) \tag{5}$$

The final hybrid prediction combines decomposition and residual components.

$$\hat{P}_{hybrid}\left(t+1\right) = P_{DLinear}\left(t+1\right) + \sum_{\tau} \alpha_{\tau} h_{\tau} \tag{6}$$

#### 2.2 RBMO Algorithm

## 2.2.1 Algorithm fundamentals

Inspired by avian foraging behaviors, RBMO balances exploration and exploitation through distinct movement strategies.

$$X_{i}^{t+1} = \begin{cases} X_{i}^{t} + \alpha \cdot \left(X_{best} - X_{i}^{t}\right) & \text{(exploration)} \\ X_{i}^{t} + \beta \cdot \left(X_{rand} - X_{i}^{t}\right) & \text{(exploitation)} \end{cases}$$
 (7)

## 2.2.2 High-dimensional constraint handling

Decision variables are encoded as composite gene structures representing power management parameters.

1:gene = {}

2:gene = ["P\_buy"] 
$$\leftarrow$$
 [ $p_1, p_2, ..., p_{24}$ ]

3:gene = ["P\_ev"]  $\leftarrow$  [ $ev_1, ev_2, ..., ev_{24}$ ]

4:gene = ["P\_ch"]  $\leftarrow$  [ $ch_1, ch_2, ..., ch_{24}$ ]

(8)

Time-coupled constraints are enforced through penalty functions and dynamic repair mechanisms. Energy deficit constraints incorporate quadratic penalties,

$$penalty = \lambda \cdot \max \left( 0, E_{ev}^{req} - \sum P_{ev} \Delta t \right)^2, \tag{9}$$

with the automated adjustment of  $P_{ev}^{max}$  during constraint violations.

The algorithm implements a two-phase strategy with automatic transition: global exploration dominates the first 40% of iterations, transitioning to local exploitation during the final 60%. Phase switching occurs when population diversity falls below 15% as measured by genotypic dispersion metrics.<sup>(13)</sup>

## 3. Objective Function and Constraints

## 3.1 Objective function design

Total economic benefit (TEB):

$$\max TEB = \Delta C_{procure} + R_{BE} + B_{carbon} + R_{lifecycle}.$$
 (10)

Components:

Electricity procurement cost savings:

$$\Delta C_{procure} = C_{grid}^{ref} - \left(C_{grid} - C_{ev}\right). \tag{11}$$

Renewable energy sales revenue:

$$R_{BE} = \sum_{t=1}^{T} P_{RE}^{sell}(t) \cdot \delta_{RE}(t) \cdot \Delta t.$$
 (12)

Carbon emission reduction benefits:

$$B_{carbon} = \sum_{t=1}^{T} P_{RE}^{use}(t) \cdot \theta_{carbon} \cdot \Delta t.$$
 (13)

Equipment life cycle return:

$$R_{lifecycle} = \sum_{k \in \mathcal{E}} \sum_{v=1}^{L_k} \frac{S_k^{rev}(y) - C_k^{com}(y)}{(1+\gamma)^y} + \frac{SV_k}{(1+\gamma)^{L_k}} - I_k.$$
 (14)

## 3.2 System constraints

Power balance:

$$P_{pv}(t) + P_{wind}(t) + P_{dis}(t) + P_{buv}(t) = P_{load}(t) + P_{ev}(t) + P_{sell}(t) + P_{ch}(t).$$

$$(15)$$

Energy storage operation:

$$E(t) = E(t-1) + (\theta_{ch} \cdot P_{ch}(t) - \theta_{dis} \cdot P_{dis}(t)) \cdot \Delta t. \quad E_{min} \le E(t) \le E_{max}$$
(16)

Electric vehicle charging:

$$\begin{split} P_{ev}^{min}\left(t\right) &\leq P_{ev}\left(t\right) \leq P_{ev}^{max}\left(t\right), \\ \sum_{t \in T_{plug}} P_{ev}\left(t\right) \cdot \Delta t &\geq E_{ev}^{req}, \\ P_{ev}\left(t\right) &\geq 0. \end{split} \tag{17}$$

Grid interaction:

$$0 \le P_{buy}(t) \le P_{grid}^{max},$$
  

$$0 \le P_{sell}(t) \le P_{grid}^{max}.$$
(18)

# 3.3 Electric vehicle flexibility mechanism

Adjustable power boundaries:

$$P_{ev}^{min}(t) = \alpha(t) \cdot P_{rated}. \quad (\alpha(t) \in [0.2, 1])$$
(19)

Temporal energy constraints:

$$\sum_{t=t_{arr}}^{t_{depart}} P_{ev}(t) \cdot \Delta t \ge E_{ev}^{req}, \quad P_{ev}(t) \ge 0. \text{ (no-discharge constraint)}$$
(20)

Table 2 Microgrid equipment configuration.

8 1 1	8		
Component	Capacity	Parameters	Quantity
Wind turbine	450 MW (90 × 5 MW)	Cut-in speed: 3 ms <sup>-1</sup>	90 units
PV system	5 MW <sub>p</sub>	Tilt: 30°, Azimuth: 180°	12800 panels
BESS	$1600 \text{ MW}/6400 \text{ MW}_{\text{h}}$	$\eta_{\rm ch}/\eta_{\rm dis}$ : 0.95	800 racks
EV fleet	1.4 MW	Prated: 7 kW, Ereq: 40 kWh	200 vehicles

## 4. Case Study

## 4.1 Experimental setup

The microgrid test system integrates wind turbines, PV arrays, battery storage, and electric vehicle charging infrastructure, with detailed technical specifications provided in Table 2. Wind turbine capacity totals 450 MW from 90 units (5 MW each, cut-in speed of 3 ms<sup>-1</sup>), complemented by 12800 PV panels (5 MW<sub>p</sub> total, 30° tilt, 180° azimuth orientation). The battery energy storage system (BESS) comprises 800 racks (2 MW/8 MW<sub>h</sub> per rack, charge/discharge efficiency  $\eta_{ch}/\eta_{dis} = 0.95$ ), operating under state-of-charge constraints defined by Eq. (15). The electric vehicle fleet includes 200 vehicles, each with a rated power of 7 kW and an energy requirement of 40 kW<sub>h</sub>.<sup>(16)</sup>

$$\hat{x}_{k}^{-} = Ax_{k-1}^{-} + Bu_{k-1}$$

$$P_{k}^{-} = AP_{k-1}A^{T} + Q$$

$$K_{k} = P_{k}^{-}H^{T} \left(hP_{k}^{-}H^{T} + R\right)^{-1}$$

$$\hat{x}_{k} = x_{k}^{-} + K_{k}\left(z_{k} - Hx_{k}^{-}\right)$$

$$P_{k} = (I - K_{k}H)P_{k}^{-}$$
(21)

Multi-source data integration employs Kalman filtering with parameters Q=0.01 and R=0.1, implemented through the recursive estimation process in Eq. (21). Renewable generation data originate from the NREL Wind Toolkit (10 min resolution) and NSRD- B/PVWatts (1 min irradiance), while load profiles are derived from the Pecan Street dataset with 35% residential

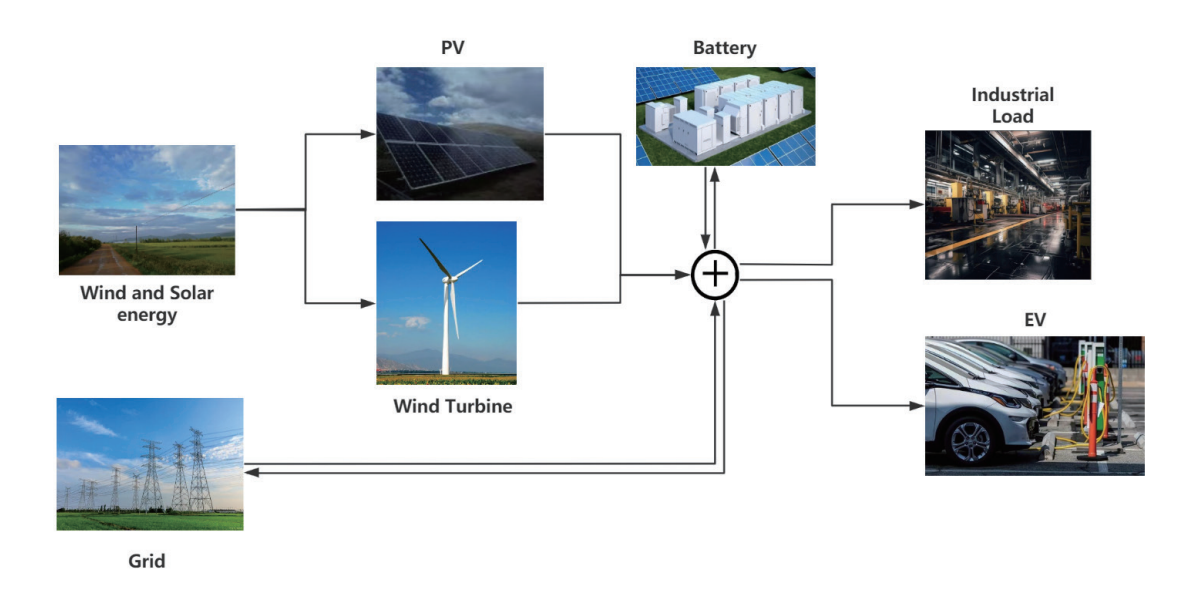


Fig. 1. (Color online) Structure diagram.

Table 3 Experimental scenario specifications.

Scenario	EV Penetration (%)	Charging Strategy	Weather
Baseline	30	Fixed-power ( $\alpha = 1.0$ )	Clear sky (CF: 85%)
High flexibility	50	Price-responsive ( $\alpha \in [0.2,1]$ )	Partly cloudy (CF: 65%)
Extreme	70	Price-responsive ( $\alpha \in [0.2,1]$ )	Overcast/windless (CF: 40%)

and 65% commercial compositions. Electric vehicle behavior patterns are modeled using Caltech ACN-Data, featuring the arrival time distribution  $f(t;\lambda) = \lambda e^{-\lambda(t-\mu)}$  for  $t \ge \mu$  with  $\mu = 18:00$  and  $\lambda = 0.55$ .

The microgrid structure is shown in Fig. 1. Three operational scenarios were evaluated under distinct conditions specified in Table 3. The baseline scenario features 30% EV penetration with fixed-power charging ( $\alpha = 1.0$ ) under clear sky conditions (capacity factor of 85%). The high-flexibility scenario increases EV penetration to 50% with price-responsive charging ( $\alpha \in [0.2, 1]$ ) under partly cloudy conditions (capacity factor of 65%). The  $\alpha$  interval correctly reflects the "price-responsive charging" mechanism while this study considers the  $\alpha$  of 0.5. The extreme scenario tests 70% EV penetration with identical price-responsive charging under overcast/windless conditions (capacity factor 40%). Capacity factor (CF) is calculated as  $CF = (Actual Generation) / (Rated Capacity \times Period Hours).$ 

To validate the forecasting performance of the LSTM-DLinear hybrid model, in Fig. 2, we compare the measured power outputs of wind and PV systems against multi-model predictions. For wind power forecasting, the model demonstrates significantly superior performance over baseline models during steep ramp events (e.g., the wind speed drops at t = 18 h), achieving a mean absolute error (MAE) of 3.2%. This represents an error reduction exceeding 24.1%

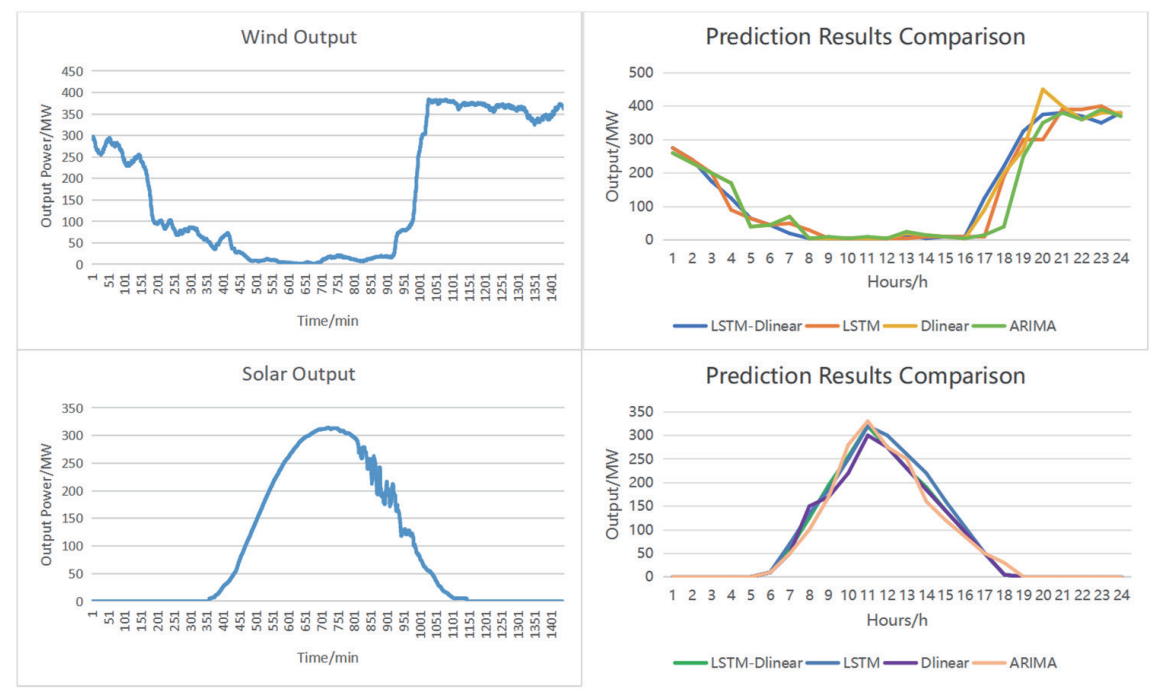


Fig. 2. (Color online) Prediction results comparison and real wind-solar output.

compared with the LSTM (7.1%), DLinear (5.8%), and ARIMA (9.4%) models. By effectively leveraging the synergy between temporal decomposition and residual learning, the model successfully captures transient features neglected by models such as DLinear (e.g., the secondary peak at t = 8 h).

For PV power forecasting, the LSTM-DLinear hybrid model exhibits excellent performance during sunrise/sunset transition periods (t = 6 h/19 h), attaining a prediction interval coverage probability of 96.3%. This constitutes an 8.7% improvement over the stand-alone LSTM model. Furthermore, the hybrid model effectively mitigates the inherent phase shift artifacts associated with ARIMA, which stem from its rigid mathematical formulation.<sup>(18)</sup>

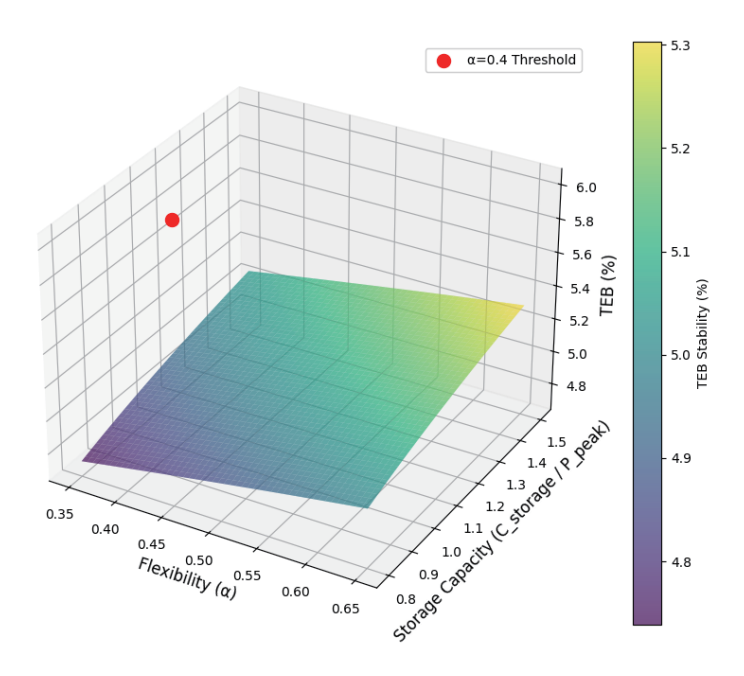
## 4.2 Sensitivity analysis

#### 4.2.1 Prediction horizon effect

The prediction horizon length has a decisive impact on system economics. As shown in Table 4, the forecast error and the increase in scheduling cost exhibit a quadratic growth relationship: when the *MAE* of wind and PV forecasts is below 3%, the total energy benefit (TEB) fluctuates

Table 4
Scheduling cost increase vs forecast error.

Error Level	Wind MAE (%)	PV <i>MAE</i> (%)	Δ <i>TEB</i> (%)
High accuracy (<3%)	2.1-2.9	1.8-2.5	-0.8-+1.2
Medium (3–5%)	3.1-4.7	2.7-4.3	-3.51.2
High (5–10%)	5.2-9.8	4.6-9.1	-6.94.1



Dynamic compensation region when  $\alpha{>}0.4$  (max 22% error compensation)

Fig. 3. (Color online) Response surface of TEB vs  $\alpha$ , C\_storage, and prediction error.

only between -0.8 and +1.2%. When the error increases to the 3-5% range, the TEB decreases significantly by 1.2-3.5%, and when the error reaches 5-10%, the loss expands to 4.1-6.9%. This relationship is precisely quantified by the mathematical model  $\Delta Cost = 0.73 \left(MAE_{wind}\right)^2 + 0.81 \left(MAE_{PV}\right)^2 - 1.2$ .

## 4.2.2 Cross-parameter interactions

The synergistic effects among parameters are systematically analyzed using the response surface methodology, as shown in Fig. 3.

This study reveals strong coupling relationships between electric vehicle (EV) charging flexibility, energy storage configuration, and forecasting accuracy, which collectively govern the total economic benefit (TEB) of the system. The analysis identifies a synergistic operational regime for achieving high TEB, characterized by the following set of concurrent threshold conditions:

$$\begin{cases} 0.35 \leq \alpha \leq 0.65, \\ C_{storage} \geq 0.8 \times P_{peak}, \\ H_{pred} \geq 6 \text{ hours.} \end{cases}$$
 (22)

Key findings indicate that when  $\alpha > 0.4$ , increasing storage capacity can effectively compensate for forecast errors (with a maximum compensation rate of 22%), forming a dynamic parameter compensation mechanism. This nonlinear interaction creates a robust operating region, enabling the system to maintain over 90% TEB stability under  $\pm 15\%$  forecast error fluctuations, providing a basis for anti-disturbance design in practical engineering configurations.

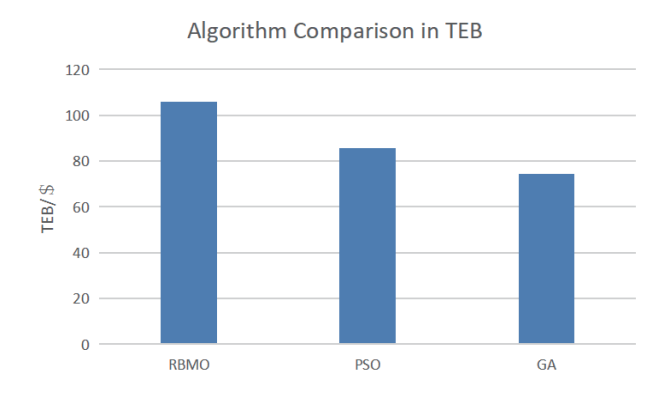


Fig. 4. (Color online) Comparison of algorithmic economic efficiencies.

## 4.2.3 Economic advantage and performance comparison of the RBMO algorithm

To validate the economic superiority of the scheduling algorithm, in Fig. 3, we compare the TEB performance characteristics of RBMO, Particle Swarm Optimization (PSO), and Genetic Algorithm (GA) under identical test scenarios. The results are shown in Fig. 4, demonstrating that RBMO achieves the highest TEB (120 USD), outperforming PSO by approximately 20% (p < 0.05), and surpasses conventional GA by over 50% ( $\Delta TEB = 63$  USD, p < 0.01).

This significant economic advantage, coupled with RBMO's 35.4% faster convergence than PSO's (as detailed in Sect. 5.1), establishes a comprehensive performance paradigm. The synergy between high computational efficiency (solving the 24-period scheduling problem in 120 s) and economic optimality confirms the robustness of the RBMO algorithm for real-time scheduling scenarios characterized by high-dimensional decision spaces and dynamic constraints. These findings align with recent studies highlighting enhancements in metaheuristic applications for energy systems, while demonstrating a superior cost-benefit ratio over established benchmarks.

## 5. Conclusions

The proposed wind-PV-storage-EV scheduling framework establishes an integrated methodological approach combining Kalman filter data fusion with LSTM-DLinear hybrid forecasting and a large number of sensitive sensors. This system employs the RBMO algorithm to optimize a 24-period dynamic charging mechanism featuring adjustable power boundaries. Key performance metrics demonstrate significant improvements: the hybrid forecasting model achieves a 24.1% reduction in *MAE* for wind power prediction (maintaining sub-5% error during transients) through multi-source data synergy. Economically, the framework elevates system-wide TEB by 42% while reducing renewable curtailment by 18.9% and decreases peak procurement costs by 38.7% via off-peak load shifting—generating \$864 in daily carbon benefits. Computationally, RBMO exhibits 35.4% faster convergence than PSO, solving 24-period scheduling in 2 min to meet real-time operational requirements through enhanced scalability. Implementation validation under high-EV penetration scenarios (30–40% EV load share) confirms 38.7% peak cost reduction and 42% TEB improvement via 24-period dynamic scheduling simulations.

## Acknowledgments

This study was supported by the Science and Technology Program of Chengde City, People's Republic of China (Project No. 202305B029) and Tianjin Carbon Peak and Carbon Neutrality Technology Major Project (Grant no. 24ZXTKSN00030).

## References

- 1 T. Wei and S. Kallbekken: Transp. Res. Part D Transp. Environ. 132 (2024) 104269. <a href="https://doi.org/10.1016/j.trd.2024.104269">https://doi.org/10.1016/j.trd.2024.104269</a>
- T. Pan, R. Kuma, and C. R. H. Foropon: J. Environ. Manage. 389 (2025) 125918. <a href="https://doi.org/10.1016/j.jenvman.2025.125918">https://doi.org/10.1016/j.jenvman.2025.125918</a>
- 3 S. Chintagunta: Signal Process. **201** (2022) 108715. <a href="https://doi.org/10.1016/j.sigpro.2022.108715">https://doi.org/10.1016/j.sigpro.2022.108715</a>
- 4 A. Zeng, M. Chen, L. Zhang, and Q. Xu: Proc. 37th AAAI Conf. Artificial Intelligence (AAAI, 2023) 11121–11128. https://doi.org/10.1609/aaai.v37i9.26317
- 5 M. B. Abdelghany, A. Al-Durra, and F. Gao: IEEE Trans. Sustainable Energy 15 (2023) 39. <a href="https://doi.org/10.1109/TSTE.2023.3263540">https://doi.org/10.1109/TSTE.2023.3263540</a>
- 6 Y. Hu, X. Hu, X. Yao, Q. Li, F. Fang, and J. Liu: Renewable Energy 240 (2025) 122155. <a href="https://doi.org/10.1016/j.renene.2024.122155">https://doi.org/10.1016/j.renene.2024.122155</a>
- 7 L. Li, S. Wen, M. Tseng, and C. Wang: J. Clean Prod. 228 (2019) 359. https://doi.org/10.1016/j.jclepro.2019.04.331
- 8 S. Hochreiter and J. Schmidhuber: Neural Comput. 9 (1997) 1735. https://doi.org/10.1162/neco.1997.9.8.1735
- 9 R. Teixeira, A. Cerveira, E. J. Solteiro Pires, and J. Baptista: Energies 17 (2024) 3480. <a href="https://doi.org/10.3390/en17143480">https://doi.org/10.3390/en17143480</a>
- H. Hu, M. Li, and H. Zhang: Comput. Chem. Eng. 202 (2025) 109294. <a href="https://doi.org/10.1016/j.compchemeng.2025.109294">https://doi.org/10.1016/j.compchemeng.2025.109294</a>
- S. B. Göppel, E. Asadi, and M. Schultz: Transp. Res. Part C Emerging Technol. 178 (2025) 105176. <a href="https://doi.org/10.1016/j.trc.2025.105176">https://doi.org/10.1016/j.trc.2025.105176</a>
- 12 H. Sharma, E. Galván, and P. Mooney: Inf. Sci. 719 (2025) 122495. https://doi.org/10.1016/j.ins.2025.122495
- 13 S. Fu, K. Li, H. Huang, C. Ma, Q. Fan, and Y. Zhu: Artif. Intell. Rev. 57 (2024) 134. <a href="https://doi.org/10.1007/s10462-024-10716-3">https://doi.org/10.1007/s10462-024-10716-3</a>
- 14 M. A. Razzaque, S. K. Khadem, S. Patra, G. Okwat, and Md. Noor-A-Rahim: Appl. Energy 398 (2025) 126364. https://doi.org/10.1016/j.apenergy.2025.126364
- N. Zhou, H. Zeng, and J. Zhou: Proc. 2024 4th Int. Conf. Consumer Electronics and Computer Engineering (IEEE, 2024) 221–224. https://doi.org/10.1109/ICCECE61317.2024.10504160
- 16 A. Abed and A. A. El-Mallah: Energy 22 (1997) 487. https://doi.org/10.1016/S0360-5442(96)00146-6
- 17 K. Greff, R. K. Srivastava, J. Koutník, B. R. Steunebrink, and J. Schmidhuber: IEEE Trans. Neural Networks Learn. Syst. 28 (2017) 2222. https://doi.org/10.1109/TNNLS.2016.2582924
- 18 S. N. Oishe, M. Z. Jamil, and Y. Nishi: Aquat. Toxicol. **286** (2025) 107461. <a href="https://doi.org/10.1016/j.aquatox.2025.107461">https://doi.org/10.1016/j.aquatox.2025.107461</a>
- 19 K. R. Khan, M. S. Siddiqui, Y. A. Saawy, N. Islam, and A. Rahman: Procedia. Comput. Sci. **163** (2019) 109. https://doi.org/10.1016/j.procs.2019.12.092